

**Mesoscale and Large-Eddy Simulation of the Boundary Layer Process of Cumulus
Development over Naqu, Tibetan Plateau
Part A: Comparison Between Simulation and Observation**

B. Kpaikpai^{1,3,5}, J. Sun^{1,2*}, J. Zhu^{2,3}, X. Huai⁴, F. Vuguziga⁶

¹Key Laboratory of Cloud-Precipitation Physics and Severe Storms (LACS), Institute of Atmospheric Physics (IAP), Chinese Academy of Sciences (CAS), 100029, Beijing, China, emilkpaikpai@mails.ucas.ac.cn, jimings@mail.iap.ac.cn, jzhu@mail.iap.ac.cn

²Key Laboratory of Geophysical Fluid Dynamics, IAP, CAS, jzhu@mail.iap.ac.cn, emilkpaikpai@mails.ucas.ac.cn

³University of Chinese Academy of Sciences (UCAS), 100864, Beijing, China, emilkpaikpai@mails.ucas.ac.cn, jzhu@mail.iap.ac.cn

⁴State Key Laboratory of Disaster Prevention and Reduction for Power Grid Transmission and Distribution Equipment (SKL), 410129, Changsha, China, huaixw@foxmail.com

⁵Togo National Meteorological Authority, P.O. Box 1505, Lomé, Togo, emilkpaikpai@yahoo.fr

⁶Key Laboratory of Meteorological Disaster of Ministry of Education (KLME), Collaborative Innovation Center on Forecast and Evaluation of Meteorological Disasters (CIC-FEMD), Nanjing University of Information Science and Technology, Nanjing 210044, China, vfloribert@nuist.edu.cn

Corresponding author: Jiming Sun (jimings@mail.iap.ac.cn)

Key Points:

- The ability of the WRF-LES model to reproduce the atmospheric boundary-layer processes of cumulus development over complex orography;
- Simulated ABL, reflectivity, and Liquid water content compared with observed Lidar measurements, radar reflectivity, and satellite image;
- WRF-LES simulations with observation nudging and one-way nesting strategies better replicated the observed clouds pattern.

Abstract

Cumulus clouds are of great interest in numerical weather prediction. However, the scarcity of observed data on the Tibetan Plateau (TP) has not allowed correct interpretation of their development. The Third TP Atmospheric Science Experiment provided experimental data to address this challenge. This study used a combined weather research and forecasting large-eddy simulation (WRF-LES) model and final reanalysis data from the Global Forecast System to simulate cumulus clouds over southern TP on July 19, 2014. We applied observation nudging and one-way nesting strategies to influence the optimality of WRF-LES runs. The study performed simulations with six different scenarios in comparison with observations data. Results showed that cumulus clouds locally initiated and grew upscale but were however influenced by large-scale forcing. Compared to the observations, simulations with observation nudging provided more accurate and reliable results than the simulations without nudging. LES with mesoscale forcing yielded a relatively good atmospheric boundary-layer (ABL) water vapor profile and a similar microphysical evolution to the observations but misled the observed surface variables. Without mesoscale forcing, LES provided the best ABL water vapor and sensible heat flux, however, failed to provide a good microphysics field. In this aspect large-scale forcing played an important role in cumulus development on July 19, 2014. The study recommended observation nudging and one-way nesting strategies in separate iterations to be improved by focusing on the model's response to the terrain and boundary conditions.

1. Introduction

The atmospheric boundary layer (ABL) processes of Cumulus Cloud (CC) development are small-scale unresolved motions and have significant effects on larger-scale resolved signals. These processes have particular consideration in numerical weather prediction (NWP) (Emanuel, 1997; Ravichandran & Narasimha, 2020). Meso- and micro-scales modeling (MMM) is being actively used to solve the physics of the ABL processes of CC development over complex terrains (Kane & Klein, 2005; Krueger, 1988; Mechem & Oberthaler, 2013), with the purpose to enrich the phenomenological basis for MMM. Unfortunately, despite an increase in computing power, the latter modeling strategy comes with a host of other challenges, such as the scarcity of observation data over complex orography to simulate the development mechanism of CC. Ultimately, the availability of appropriate boundary conditions to replicate the development of the ABL processes (P. Ray, 2015) is a limit to MMM.

As such, Tibetan Plateau (TP) region is one of the most complex terrains in the world. Human life and the ecosystem of South East Asia (SEA) depend on water from the major rivers such as the Brahmaputra, Ganges, Irrawaddy, Mekong, Salween, Yangtze, and Yellow River, which headwaters are located on TP. The water supply in these rivers is strongly related to the ABL processes of the cumulus convection that further produces precipitation fall (Zhao et al., 2018, 2019). In addition, the ABL processes over TP are well known to hydrating the global atmosphere (R. Fu et al., 2006; IPCC, 2014). However, the predictability of the latter process on TP relied on sparse and scarce observations that did not provide the required accuracy, spatial density, and temporal frequency (Y. Liu et al., 2020; Zhao et al., 2019), posing difficult challenges when applying numerical modeling to understand the CC development in that region. The latest campaign work, the Third TP Atmospheric Science Experiment (TIPEX-III), conducted from July 1 to August 31, 2014 (L. Liu et al., 2015; Zhao et al., 2018, 2019), provided comprehensive experimental data, which motivated our interest in studying ABL process of CC development over Naqu in south TP (STP).

Typically, CCs are detached and dense, with sharp outlines. They develop vertically in the form of rising towers. CCs often begin to form in sunny and fair weather as soon as the ascending air cools to the point where vapor becomes supersaturated. Subsequently, the water vapor condenses into liquid water droplets or solid ice crystals. Congestus CCs may turn into cumulonimbus and produce thunderstorms when influenced by mesoscale instability, humidity, and temperature gradient. Cumulonimbus grows vertically and may penetrate at greater heights from 300 to 12,000 m AGL (Cotton & Anthes, 1992). The large CCs and thunderstorms are classified into meso- γ atmospheric processes (Anthes, 1986; Cotton & Anthes, 1992; Emanuel, 1993; Fujita, 1986). CCs are precursors of other cloud types, while meteorologists may refer to CCs underway to determine the kind of weather that will occur. However, the ABL processes of CC developments have limited predictability due to uncertainty associated with the initial conditions. According to the Fifth Assessment Report of the Intergovernmental Panel on Climate Change (IPCC, 2014), the numerical representation of the ABL clouds is an open problem in cloud modeling. This points out a need for the numerical study of ABL clouds development.

The broad classes of mesoscale phenomena influencing the ABL processes of CC development are the internally and externally forced-mesoscale processes. The former class derives structure and circulation within the atmosphere. The latter class results from the earth's

surface–atmosphere interaction, including either thermal forcing due to the differential heating of the coupled earth’s surface–atmosphere, or mechanical forcing due to the atmospheric response to the irregular topography (Arya, 2001; T. Wang et al., 2002; Wu et al., 2007). Each area of TP, including STP, has particular ABL processes of CC development, interacting with large–scale forcing. The diurnal surface heating over TP in summer reflects an external forcing element, which interacts with a large–scale forcing, and mesoscale moisture transport then influences the ABL process of cumulus development. There is fifty years back, (Flohn, 1968) highlighted that during the summer the TP act as a heat engine with an enormous convective chimney in the southeastern sector where giant cumulonimbus cells play a major role in continuously carrying heat upward into the high troposphere. Li et al., (2010) and Ding et al., (2018) revealed that warm and wet events have notably increased over the region and altered hydrological processes (X. Liu et al., 2006; J. Wang et al., 2020). As a result, various weather conditions influence billions of people living in the SEA region, particularly in the downstream sector (Lei et al., 2021; T. Wang et al., 2002; K. Yang et al., 2004).

The effect of the diurnal temperature variation on TP has been observed in the diurnal evolution of the TP’s ABL structure, the most characteristic in the world. In dry and warm land surface–atmosphere conditions, the top of the ABL over TP could reach approximately 5 km of mean height AGL, higher than any reported ABL worldwide while a shallow ABL top is observed only about 2 km mean of height AGL in the moist condition of the coupled system (Ao et al., 2017; Chen et al., 2013, 2016; Y. Li & Gao, 2007; Sato, 2009; Yanai & Li, 1994; Zhao et al., 2018). According to previous studies, ABL on TP exerts a profound thermal and dynamic influence on the cumulus development (Chen et al., 2016; Y. Li & Gao, 2007; Slättberg & Chen, 2020; K. Yang et al., 2004). Many studies showed that the radiative budget of the ABL has a direct effect on the variation in CC cover (Ao et al., 2017; Betts & Ball, 1994; Margulis & Entekhabi, 2004). However, the upper–level potential vorticity structures and the meridional position of the subtropical jet (STJ) also influence the feature of the ABL on the TP (Chen et al., 2016). In midsummer, STJ and the South Asian High (SAH), coexist and intensify the upper–level subsidence in some STP’s zones, characterized by less cumulus development (Chen et al., 2016; Sato, 2009). The mean position of the STJ was 40° north between 1979 and 2003 (Sato, 2009).

From the 1970s to 2014, three scientific experiments, including TIPEX-III, promoted the understanding of the cloud processes on TP (Y. Fu et al., 2020; L. Liu et al., 2015; Zhao et al., 2018, 2019). However, the pursuit of in-depth knowledge of water and energy cycles on TP still raises questions related to multi-scale CC interactions. Three decades ago, Tingyang & Reiter, (1990) found that the condensation rate of water vapor in clouds, the clouds’ liquid water content (LWC), and the precipitation efficiency in clouds are lower than those in surrounding regions through observation analysis and model simulations. Based on CloudSat and Cloud-Aerosol Lidar and Infrared Pathfinder Satellite Observations (CALIPSO), (Luo et al., 2011) further showed that CC convections were shallower over TP than those over the other two subregions of the TP–South Asian monsoon region. By contrast, the TIPEX-III campaign work revealed that most congestus CCs developed on TP, preferably in the afternoon, some of which penetrated vertically as high as 16.5 km AGL (L. Liu et al., 2015; Zhao et al., 2018).

Most studies mentioned above focused on model simulations of the large-scale and mesoscale cloud processes on TP (Couvreur et al., 2009; Gao et al., 2016; Larson et al., 1999;

Tingyang & Reiter, 1990; K. Yang et al., 2004). In line with this, Fu et al., (2020) reviewed the progress of land-atmosphere interactions on TP. The authors suggested conducting an observational analysis coupled with numerical simulations to further understand the effect of ABL processes. Couvreur et al., (2009) pointed out that ABL water vapor variability is the main trigger of mesoscale convective clouds. Accordingly, this study analyzed the ABL features that may influence CC development.

Because of the extensive limitations in understanding the cloud processes on TP, Gao et al., (2016) showed that clouds and precipitation over TP have not been studied sufficiently due to the lack of observations over the harsh mountainous areas and the poor representation, in NWP models, of the CC processes over TP. Many studies emphasized that many modeling studies of CC processes on TP were probably inadequate to capture the complex interactions of the physical processes (Gao et al., 2016; L. Liu et al., 2015; Zheng et al., 2015, 2016). Sato, (2009) investigated the resolution dependency of the diurnal cycle of convective clouds on TP in a mesoscale model. They pointed out that convective clouds over TP during the day tend to have a small horizontal scale rather than a resolvable mesoscale resolution, and suggested further study with finer resolutions of less than 7 km. However, they did not specify how fine is enough to resolve the inaccuracy associated with the orography feature. With advances in the application of the coupled WRF-large eddy simulation (WRF-LES), it is now easy to understand the link between multi-scale CC development and determine the dominant trigger of CCs (Chow et al., 2005; Takemi & Rotunno, 2003; Zhu et al., 2010).

This study answered the question of how the model can reproduce the CC process by performing six scenarios with WRF-LES in a real-case mode. To this end, this study organized the other steps as follows: Section 2 describes the experimental data and modeling framework. Section 3 gives a comparison between the simulation and observation. The summary and conclusions are presented in Section 4.

2. Data, Modeling Framework

2.1. Experimental Data

The study used the TIPEX-III dataset from 8 meteorological stations, where the surface measurements and L-band radiosonde soundings were used as input for the observation nudging to improve the initial and lateral boundary conditions (LBCs) and gradually adjust the model state toward observations during its integration. The purpose was to link the model's prognostic variables to the observed quantities to capture the atmospheric flow around the Naqu area, including Naqu1 and Naqu2. We can approximate the distance between Naqu1 and Naqu2 stations as 5.4 km. The stations consist of active remote sensing sites, automatic meteorological towers, ABL towers, and 2 surface weather observation stations, Naqu Plateau Cold Climate and Environment 1 and 2 (NPCE1 and NPCE2). These stations follow the recommendations of WMO, and all data from TIPEX-III are quality controlled before publication. The measurement devices used during TIPEX-III included operational radiosondes, cloud radars, laser ceilometer 31 (CL31), and other in situ observation devices. The Cold and Arid Regions Environmental and Engineering (CARE) research institute and the Chinese Academy of Sciences (CAS) support these stations in providing unique observation data. The data are distributed by the China

Meteorological Administration (CMA). Liu et al., (2015) describes most devices used during the TIPEX-III.

Table 1. Experimental data stations; asterisks indicate sounding sites; double asterisks indicate the source of radar reflectivity; AGL, above ground level.

Station Name	Longitude	Latitude	Station Height (m) AGL	Station ID
LHASA*	91.133	29.667	3649	55591
LINZHI*	94.340	29.667	2992	56312
NAQU1*	92.067	31.483	4508	55299
NAQU2**	92.01	31.48	4507	55299
NPCE1	91.900	31.300	4534	-
NPCE2	90.900	31.300	4508	-
RIKAZE*	87.080	28.633	4302	55664
YITUOHE*	92.433	34.210	4534	56004

2.1.1. Surface and Tower-Based Measurements

Surface measurements from NPCE1 and NPCE2 and tower-based measurements from Naqu1 include air temperature (T), relative humidity (RH), air pressure (P), vapor pressure (e), and wind speed (U_z). Tower-based measurements were available at 0.75, 1.5, 3, 6, 12, and 22 m AGL. Data from each site were time series recorded from July 17 to 20, 2014. Each item in the series represents the mean of the data recorded over a 30-min period. The tower-based measurements were used to compute the mean wind speed U_z , the potential temperature difference $\Delta\theta = \theta(T_z) - \theta(T_s)$, and specific humidity difference $\Delta q = q_s - q_z$, where subscript s represents 0.75 m AGL and z represents 3 m AGL for temperature and specific humidity, and 12 m AGL for wind speed. This study estimated HFX and the latent heat flux (LH) as given in Equations (1) and (2) (Gavilán & Berengena, 2006; Verma et al., 1986):

$$\text{HFX} = C_H \cdot \rho_a \cdot C_p \cdot U_z \cdot \Delta\theta \quad (1)$$

$$\text{LH} = C_E \cdot \rho_a \cdot L_v \cdot U_z \cdot \Delta q \quad (2)$$

where $L_v = 2.501 - (2.361 \cdot 10^{-3}) \cdot T$ is the latent heat of vaporization, C_p is the specific heat of the air, ρ_a is the mean air density, and C_H and C_E are the bulk transfer coefficients for heat and moisture, respectively. The estimation was done assuming the bulk transfer coefficients equal to the drag coefficient (C_D). Li et al., (1996) and Zhao et al., (2018) found $C_D = 4.4 \cdot 10^{-3}$ for the Naqu area, and there was no need to perform this calculation in this study.

2.1.2. L-Band Radiosonde Sounding Measurements

The L-band radiosonde sounding stations are indicated with an asterisk in Table 1. The variables used in this study include air temperature, wind speed, wind azimuth, air pressure, relative humidity, and geographical height. The data were recorded each minute for about 1.5 hours and were available at the predetermined synoptic times, except on July 18, 2014, where 3 soundings were launched, at 0615UTC, 1115UTC, and 2315UTC, over Naqu1. Wind speed and

azimuth were used to decouple the wind field into meridional and zonal wind components. The latter was used as input for observation nudging.

2.1.3. Automatic Laser Ceilometer Measurements

The ABL height data were determined over Naqu2 with a Vaisala CL31 automatic laser ceilometer. The CL31 has a time resolution of 16 s and a vertical resolution of 5 m. The CL31 used in this study is a mini-Lidar made in Finland and maintained by China Ocean University. The CL31 is used for active remote sensing measurements to characterize the ABL height with the backscatter signal and has good accuracy (Kotthaus & Grimmond, 2018; Sokół et al., 2014). This study used the measurements from the CL31 as a reference for the simulated ABL. The purpose of using the CL31 measurement was to avoid a false ABL depth estimation.

2.1.4. Ka-Band Millimeter-Wave Radar and Fengyun 2D Satellite Images

The cloud row data were determined over Naqu2 using a Ka-band millimeter-wave cloud radar. The device has a time resolution of 0.85 s and a vertical resolution of 30 m. The data from July 19, 2014, were used to retrieve the radar reflectivity. The radar reflectivity mentioned here is a measure of the fraction of the precipitation intensity reflected from the cloud surface. The millimeter-wave cloud radar data browsing software, HMB-Disp, provided by Naqu2 was used to extract the radar reflectivity. Visible light 2D images from the Fengyun (FY-2D) geostationary meteorological satellite at 16:45 local standard time (LST) on July 19, 2014, were also used as a reference to simulated reflectivity. The original data has a horizontal resolution of 5600×4800 pixels.

2.2. WRF Modeling Framework

2.2.1. WRF Model Description

The WRF model is a non-hydrostatic, compressible atmospheric model, which is the most widely used in NWP for research and operational needs (Powers et al., 2017). The WRF model has grid nesting capability, which allows simultaneous multiscale simulation (Powers et al., 2017; Skamarock et al., 2008). The model has several initialization programs for idealized and real-data simulation cases and provides several parameterization options, such as land surface, surface layer, planetary boundary layer (PBL), microphysics, CC parameterization (Gentry & Lackmann, 2010), and adaptive subgrid-scale (SGS) mixing parameterization (Canuto & Cheng, 1997; Y. Liu et al., 2011; Takemi & Rotunno, 2003). In this model, the turbulent kinetic energy and non-local closure schemes enable the PBL to develop with entrainment (Dai et al., 2014; Dudhia, 2014; Shin & Dudhia, 2016; Skamarock et al., 2008).

As mentioned above, the WRF model has more computing power and allows the coupled WRF-LES to perform real case simulations at meso- and micro-scales resolutions (Y. Liu et al., 2020; Talbot et al., 2012). The purpose of applying the LES is to implicitly calculate the small-scale turbulence from the flow field and explicitly resolve the largest scales of energy production, while the basis of the LES strategy in the WRF model is low-pass filtering (Chow et al., 2005; Chow & Street, 2009; Mirocha et al., 2010; Shin & Dudhia, 2016). The application of

coupled WRF-LES in real case mode uses a surface layer scheme to connect the lower boundary and the atmosphere.

Table 2. Five nesting domains, $\Delta x_{i=1-5} = \Delta y_{i=1-5}$, represent grid spacing (m) where i ranges from 1 to 5 to represent the domains $D0_{i=1}$, $D0_{i=2}$, $D0_{i=3}$, $D0_{i=4}$, and $D0_{i=5}$; $\partial t(s)$, the time step in seconds; \mathcal{A} is the area of the domain (km^2).

Mesoscale Simulation Runs				
Simulation Type	$\Delta x_{i=1-5} = \Delta y_{i=1-5}$ (m)	Horizontal Grids Points	\mathcal{A} (km^2)	$\partial t(s)$
$D0_{i=1}$ Mesoscale- γ	9,234	150×150	1385.1×1385.1	15
$D0_{i=2}$ Mesoscale- γ	3,078	150×150	461.7×461.7	5
$D0_{i=3}$ Microscale- α	1,026	150×150	153.9×153.9	5/3
Large-Eddy Simulation Runs				
$D0_{i=4}$ Microscale- α	342	150×150	51.3×51.3	3/20
$D0_{i=5}$ Microscale- β	114	150×150	17.1×17.1	1/20

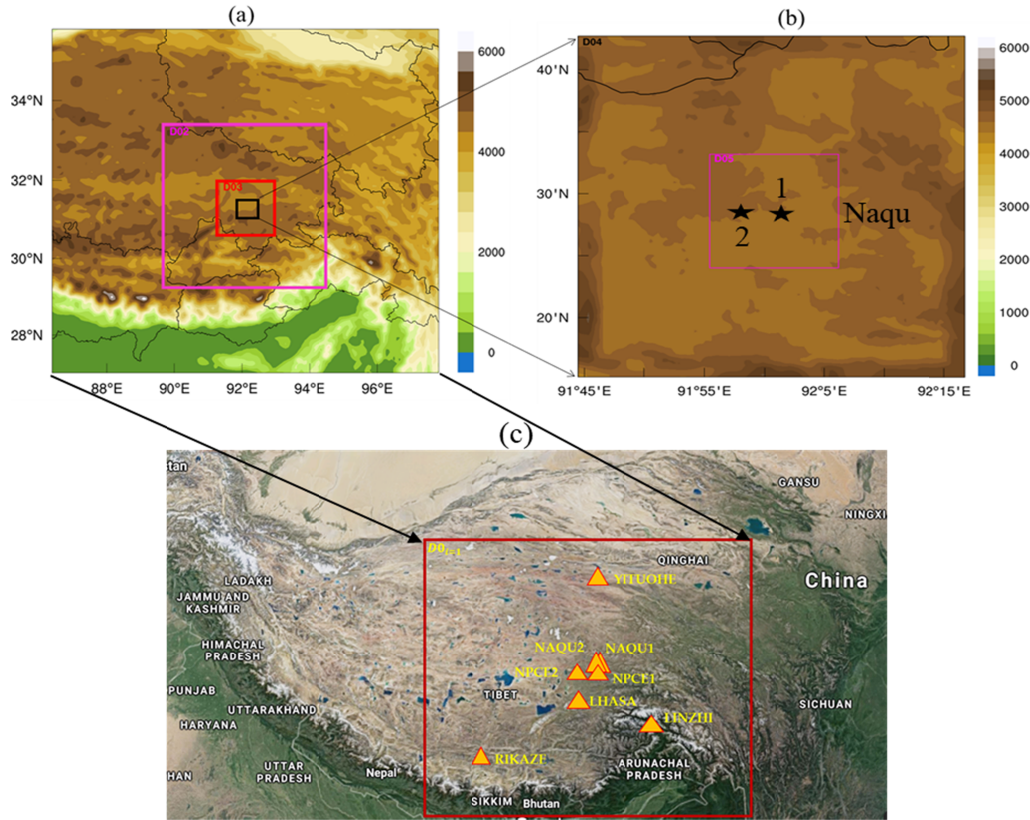


Figure 1: WRF domain configuration: (a) mesoscale domains, (b) microscale domains; shaded area represents terrain height (m) above sea level (ASL). The black stars 1 and 2 are respectively the Naqu1 and Naqu 2 stations (c) google map with yellow triangles indicating the location of each station.

The coupled WRF-LES is constructed by applying a one-way nesting strategy in two separate iterations. This strategy is an option in the WRF model, defined as a finer-grid-resolution run. This strategy is used as a subsequent run after the coarser-grid-resolution run, where the program (ndown) is run in between the two simulations. The coarse-grid run provides

the initial and lateral boundary conditions (LBCs) to the finer-grid run, with data from higher-resolution land and masked surface fields. The latter strategy only feeds suitable information from the outer domain to the inner one. The one-way nesting strategy has been used in many studies with good results (Chow & Street, 2009; Y. Liu et al., 2011; Moeng & Wyngaard, 1989; Soriano et al., 2004; Zhu et al., 2010).

Soriano et al., (2004) suggested that for mesoscale simulation runs, the one-way nesting technique should be used because two-way nesting gave the worst results in their case study. Zhu et al., (2010) suggested that using one-way nesting runs allows simulation of complicated and heterogeneous forcings, and recommended that this strategy be used for cloud cases that require extremely high resolution.

The WRF model system also includes the observation nudging strategy used in this study. This strategy uses Newtonian relaxation to improve either the dynamics initialization or analysis, respectively (Cheng et al., 2009; Reen et al., 2016; Yesubabu et al., 2014). However, assimilation of moisture fluxes may pose particular difficulties when applying observation nudging due to the high spatial variability of the variables such as the water vapor mixing ratio and specific humidity relative to their absolute values (Reen et al., 2016). For simplicity, this study applied observation nudging to wind and temperature to avoid excessive drying that can be caused by negative water vapor values occurring within the model domain.

2.2.2. WRF Model Domain Configuration

This study used version 3.8 of the WRF-ARW dynamical solver installed on the Tianhe high-performance computing (HPC) system and assisted by the Sugon HPC system from the State Key Laboratory of Disaster Prevention and Reduction for Power Grid Transmission and Distribution Equipment (SKL) at Changsha, China. To get a suitable design for the multiscale atmospheric reanalysis, we designed 5 WRF model domains, $D0_{i=1-5}$, where $D0_{i=1} = D01$, $D0_{i=2} = D02$, ..., $D0_{i=5} = D05$ by assigning $D0_{i=1-3}$ to mesoscale simulations, and 2 microscale domains $D0_{i=4,5}$ all in $D0_{i=3}$, assigned to LES runs. The model domain configuration is given in Table 2 and depicted in Figure 1. As shown in Figure 1a, Naqu1 is the center of all domains. The parent domain $D0_{i=1}$ includes China's 6 administrative prefectures, Naqu, Linzhi, Lhasa, Rikaze, Shannan, Chamdo, and Yituohe, and neighboring southern countries. As shown in Figure 1b, $D0_{i=4}$ was configured to cover Naqu1 and Naqu2 observation stations, while Naqu1 is the center of $D0_{i=5}$.

As shown in Table 2, each domain has 150 horizontal grids. In this configuration, the innermost domain has 114m horizontal grid resolution with an area of $114 \times 114 \text{ km}^2$ including Naqu1 and Naqu2. In this configuration, some vertical layers was set to 50 full sigma levels up to 50 hPa, except in one scenario namely scenario B1 wherethe vertical levels have been increased and reorganized manually to be many within the ABL. In the domain configuration for scenario B1, the vertical layers are composed of 56 full sigma levels up to 50 hPa, while the vertical increment $\Delta z_{i=0-55}$ between two consecutive levels increased linearly following the hyperbolic cosine function:

$$\left\{ \Delta z_i = Ch(\lambda_i) = \frac{e^{\lambda_i} + e^{-\lambda_i}}{2}; \lambda_{i=0-55} \in [2.797324366; 8.217039] \right\}$$

In the latter configuration, the first model level's height is 8 m AGL, while the first 40 model levels are below 4000 m height AGL (~ 300 hPa). The domain $D0_{i=3}$ provides the initial conditions for $D0_{i=4}$ to optimize LES results. The horizontal and vertical interpolations are performed with an overlapping quadratic approach and linear log pressure, respectively. These interpolations allow the boundary forcing to vary in time and space. Mesoscale simulations use 1D PBL parameterization to fully parameterize the anisotropic turbulent motion using the Reynolds-averaged Navier–Stokes (RANS) technique (Powers et al., 2017), whereas LES runs treat unresolved isotropic turbulence using SGS schemes (Chow & Street, 2009; Deardorff, 1980; Moeng & Wyngaard, 1989; Shin & Dudhia, 2016; Takemi & Rotunno, 2003). In fact, different ranges of scales from microscale to mesoscale must be solved to obtain a complete representation of the superimposed physical mechanisms involved in the ABL process of CC development. However, in the coupling model domain configuration, there is a range of grid resolutions where certain processes are neither sub-grid nor resolved, the so-called “grey zone” or “terra incognita”. These domains may be considered either mesoscale using 1D PBL or microscale requiring LES strategy. The test experiment of (Talbot et al., 2012) successfully used $D0_{i=4} = 450\text{m}$ for LES runs of the ABL. This study increased the resolution for $D0_{i=4}$, be closer to the LES standard.

Our study focused on ABL processes of CC development on July 19, 2014. However, all simulations were performed over 72 hours from July 17 to 20, 2014. This is because TP is at a very high altitude and has complex orography, which causes the model to be statically unstable. Therefore, after several text experiments, this study assumed that 24 hours are enough to assess the effect of the model’s spin-up during model domain initialization. The history interval was set to 15 minutes to create high time resolution data. We recorded 48 hours series (from day 2 to day 3) for model evaluation.

The traditional United States Geological Survey dataset (USGS) collected from 1992 to 1993 was applied to account for the influence of terrain and its related water bodies on WRF-LES surface heat fluxes and meteorological variables. This study selected USGS 30 arc-second (~ 900 m) Details on the data are given at the USGS website (<http://www.usgs.gov/>). Liu et al., (2020) and Sertel et al., (2010) demonstrate that the use of the default WRF dataset may cause misrepresentation of the study region, while, there are spectral mixing problems between classes in land use. Therefore, this study tested the high-resolution Shuttle Radar Topography Mission (SRTM) dataset, 3 arc-second ($\sim 90\text{m}$) for comparison with USGS dataset (Not shown). The data can be downloaded at (<http://www2.jpl.nasa.gov/srtm/>). However, there needed to be no improvement with SRTM dataset. Some simulation results can be seen in Figure 1 of the supplementary file.

Initial and lateral boundary conditions were generated from the National Centers for Environmental Prediction (NCEP) Final Analysis (FNL) derived from the Global Forecast System (GFS) and were accessed on September 05, 2019. FNL data have a resolution of $1^\circ \times 1^\circ$ grids at six-hourly time steps with 26 vertical levels from 10 to 1000 hPa of isobaric surface data and can be downloaded at <https://doi.org/10.5065/D6M043C6>.

2.2.3. Flow Parameterization Options

This section gives details of the parameterization schemes used in this study and describes the experimental design. It also presents the one-way nesting strategy that coupled mesoscale simulations with microscale one. Table 3 summarizes the parameterization options. As shown in Table 3, the coupled land-atmosphere fluxes were computed using the Unified Noah Land Surface Model (Niu et al., 2011; Z.-L. Yang et al., 2011). Surface boundary conditions used Monin–Obukhov logarithmic similarity theory to prescribe fluxes of heat, moisture, and momentum (Chen et al., 1997; van den Hurk & Holtslag, 1997; Jiménez et al., 2012). The Mellor–Yamada scheme (Janjic, 2002) was selected for mesoscale simulations to account for turbulent kinetic energy (TKE) in local vertical mixing. The Thompson scheme was selected to parameterize the microphysical process. Short– and longwave radiation were integrated from the radiative transfer scheme (RRTMG) (Iacono et al., 2008; Mlawer et al., 1997). Kain, (2004) (hereafter referred to as KF) proposed a deep and shallow CC convection scheme, which was selected to resolve CC processes only in domain $D0_{i=1}$. Jeworrek et al., (2019) suggested combining the KF and Thompson microphysics schemes to improve the high-resolution numerical simulation results. However, the KF scheme was useless for $D0_{i=2-5}$, respectively, because these domains fell into the grey zone. On the other hand, a test simulation with the KF scheme in LES runs provided too much precipitation. Some pictures are shown in Figure 3 of the supplementary file.

Table 3: Summary of flow parameterization. SGS, subgrid-scale; $D0_{i=1-5}$.

Parameterization options	Mesoscale domains			Microscale domains	
	$D0_{i=1}$	$D0_{i=2}$	$D0_{i=3}$	$D0_{i=4}$	$D0_{i=5}$
Cumulus	Kain–Fritsch	Useless			
Planetary boundary layer	Mellor–Yamada			Real case LES mode	
Surface layer	Monin–Obukhov				
Land-surface	Unified Noah LSM				
Cloud microphysics	Thompson				
SGS stress model	Useless			TKE1.5	

For the real–case LES in the high mountain range, the recommended SGS turbulence model is a 1.5–order of TKE energy (TKE1.5) closure model (Skamarock et al., 2008). The TKE1.5 model accounts for diffusive transport of the TKE and allows more uniform diffusivity and entrainment through the convective ABL (Canuto & Cheng, 1997; Chow & Street, 2009; Y. Liu et al., 2020; Zheng et al., 2015). In real–case LES mode, the use of SGS TKE1.5 needs a filter (C_k) in the inertial subrange to filter the SGS noise (Deardorff, 1980; Takemi & Rotunno, 2003). The filter was set to a default value ($C_k = 0.15$) in this study. The advection options of order $O(h) = 5$ and $O(h) = 3$ were used to compensate for the coarser horizontal resolution (Skamarock et al., 2008).

2.2.4. Experimental Design

We designed six scenarios (case experiments A, B, B1, C, D, and E), based on Talbot et al., (2012) and Heinze et al., (2017), to account for the reliability of simulation results compared to observations, the efficiency of physical parameterization, and the skill of the strategy used in each scenario. These allowed us to prescribe dynamics associated with ABL process of CC development over TP. We first assessed the mesoscale simulations, then performed the LES runs through a one-way nesting strategy, as presented in Table 4.

Table 4. : Controlled experiment for mesoscale simulations and LES; observation data were used through Observation Nudging strategy; FNL, final reanalysis; TKE1.5, one and a half order turbulent kinetic energy closure model, used in anisotropic turbulence for mesoscale simulations and isotropic turbulence for LES; $R_{i=1-3}$ represent the radii of influence values from $D0_{i=1}$ to $D0_{i=3}$, and $R_{i=4,5}$ are the values from $D0_{i=4}$ to $D0_{i=5}$, Eta levels were generated automatically for cases A, B, and C but customized for case B1. SGS, subgrid-scale.

Mesoscale Simulations	Case	Input Data	Horizontal Turbulence	Eta levels	Horizontal Grid Spacing $\Delta x_{i=1-3} = \Delta y_{i=1-3}$ and $R_{i=1-3}$		
					$D0_{i=1}$ $\Delta x1 = \Delta y1$ =9,234 m	$D0_{i=2}$ $\Delta x2 = \Delta y2$ = 3,078 m	$D0_{i=3}$ $\Delta x3 = \Delta y3$ = 1,026 m
	A	FNL	TKE1.5	50, 1rst model level: 65 m with 16 layers < 4000m	R_1 is useless	R_2 is useless	R_3 is useless
	B	FNL, Obs.		56, 1rst model level: 8 m with 40 layers < 4000m	$R_1 = 980,000$ m	$R_2 = 330,000$ m	$R_3 = 120,000$ m
B1							
Microscale Simulations	Case	Input Data	Parent Mesoscale Turbulence Model	SGS Turbulence Model	Horizontal Grid Spacing $\Delta x_{i=4,5} = \Delta y_{i=4,5}$ and $R_{i=4,5}$		
					$D0_{i=4}$ $\Delta x4 = \Delta y4$ = 342 m	$D0_{i=5}$ $\Delta x5 = \Delta y5$ = 114 m	
	C	Input from case B, FNL, and observation	TKE1.5	TKE1.5	$R_4 = 40,000$ m	$R_5 = 15,000$ m	
	D	Observation and FNL	The parent mesoscale turbulence model (TKE1.5) is useless				
E	FNL						

As presented in Table 4, we designed a mesoscale simulation, scenarios A as a benchmark experiment to help determine the optimality of observation nudging in scenario B. We applied observation nudging in scenarios B, B1, C, and D. The nudging strength in these simulations was set to $120 \times e^{-4} s^{-1}$. As shown in Table 4, the radii of influence were set to $R_{i=1-5}$, respectively for $D0_{i=1-5}$. Each radius of influence on a given domain was slightly greater than a half-diagonal of that domain. Therefore, each point of the WRF domain at any distance within the domain will be influenced at least by one observation station. Observation stations are less dense and sparse (Figure 1c). We wanted every observation at any station to influence the whole domain at maximum. Therefore, scenario B determines the impact of observation nudging on the simulation results. Scenario B1 determines the optimality of the external forcing on the ABL such as surface drag and heating caused by the infrared radiation divergence imposed to the

atmosphere. Note that surface characteristics directly affect ABL. Therefore, increasing the layers in this part accentuates the effect of surface characteristics on the simulation results. Scenario C is an LES that determines the effect of large-scale forcing on microscale circulation. LES is useful for understanding the specific processes underlying the ABL, clouds, etc. In this scenario, a one-way nesting strategy was performed between $D0_{i=3}$ and $D0_{i=4}$ where the former provides the boundary condition for the latter with data from higher resolution land and masked surface fields. As mentioned earlier, this strategy only feeds suitable information from $D0_{i=3}$ to $D0_{i=4}$ and there is no feedback between these two domains. Scenario C differs from scenario D only by the use of the one-way nesting strategy. Indeed, scenario D is a control experiment for scenario C, which helps to determine the optimality of applying the one-way nesting strategy. We designed the scenario E as a benchmark experiment for LES run to help determine the optimality of observation nudging in scenario D. The vertical resolution has not been tested for scenarios C, D, and E due to their very high computational cost. Briefly, in this approach, we focused on scenario B to achieve our objective of using observation nudging. Scenario C utilized the input from scenario B as the boundary condition, and we were expecting the scenario C to reproduce the results from B but is much improved. A study by Heinze et al., (2017) successfully used the same approach to evaluate the mean ABL quantities and turbulence statistics.

2.2.5. Evaluation metrics

The model evaluation is based on the mean bias (MB) and the root mean squared error (RMSE) statistics (Stanski et al., 1989; Willmott et al., 1985) as given in Equations (12) and (13), respectively:

$$\mathbf{MB} = \frac{\sum_{j=1}^n (f_j - o_j)}{n} \quad (12)$$

where $f_{j=1,...,n}$ are the simulated values from the model, $o_{j=1,...,n}$ are the observation values, and n is the number of data points used in the calculation; and

$$\mathbf{RMSE} = \sqrt{\frac{\sum_{j=1}^n (f_j - o_j)^2}{n}} \quad (13)$$

Mean bias represents a gross measure of reliability, while RMSE represents a measure of the spread of differences between the forecast and observed values with the same units of measurement.

3. Comparisons Between Simulations and Observations

3.1. Model Evaluation Results

The evaluation scores are shown in Table 5, and Figures 2a,d illustrates the time series used for model evaluation. We considered the period after 24 hours of spin-up time for evaluation, that is from day 2 to 3. Table 5 shows that WRF-LES had a general tendency to overestimate the observation field except for the temperature, where the model underestimated the observation in all scenarios.

Table 5 shows that scenario A has a more accurate result in temperature than those in other simulations. The lowest score value is 1.8 K for RMSE. The largest values found in scenario A are LH scores of 61.64 w/m³ for MB and 72.21 w/m³ for RMSE. Large LH indicates large precipitation. As shown in Table 5, scenario B overestimated the observation except for the temperature. However, it tended to record the best lowest score values for wind speed (0.16 m/s for MB and 1.05 m/s for RMSE) and LH (69.57 w/m² for RMSE). The release of LH plays a role in heating the air, which rises. The air cools while the water vapor condenses, gradually forming clouds. Therefore, scenario B should provide the best distribution of cloud patterns compared to observation.

The scenario C, as shown in Table 5 overpredicted the observation, with a tendency to record the largest score values, especially for WSD (4.89 m/s for MB, 5.94 m/s for RMSE) and LH (61.98 w/m² for MB and 111.44 w/m² for RMSE). As mentioned earlier, WRF-LES overestimated observation in LH and predicted excessive precipitation. From the visual inspection, unexpected high wind speed values in scenario C (Figure 2a) contributed to high LH. Thus, the overprediction of wind speed in scenario C may be related to lateral boundary noise in the WRF-LES model runs, specifically when using a one-way nesting strategy in separate iteration steps. In fact, the one-way nesting strategy in separate iterations for the wind speed simulation over unresolved topography may increase errors in simulation results.

As shown in Table 5, scenario D provided a more accurate result in HFX compared to other scenarios, with the lowest score value of 40 w/m³. Also, scenario D had reliable results in temperature and LH, with the lowest score values of -0.16 K and 44.98 w/m³, respectively. Referring to a study by Zhao et al., (2018), WRF-LES runs in scenario D can predict the best ABL because it has better results in HFX.

Table 5: The mean bias (MB) and the root mean square error (RMSE) for two-meter temperature (T2), 10 m wind speed (WSD), the sensible heat flux (HFX), and the latent heat flux (LH); four scenarios are denoted as cases A, B, C, and D. $D0_{i=3}$ is the third domain and $D0_{i=5}$ is the fifth domain.

Score	Boundary-Layer Variables	Case A	Case B	Case B1	Case C	Case D	Case E
MB	Temp (K)	-0.41	-0.42	-0.15	-1.01	-0.16	2.02
	WSD (m/s)	0.83	0.07	1.32	4.75	4.56	3.80
	HFX (w/m ²)	42.24	37.88	19.26	-4.57	-23.87	-5.50
	LH (w/m ²)	61.64	56.26	97.41	-21.36	44.98	78.59
RMSE	Temp (K)	1.8	1.86	2.83	3.31	3.11	3.12
	WSD (m/s)	1.56	1.20	3.12	6.27	6.14	5.20
	HFX (w/m ²)	56.89	53.62	56.54	44.07	40.00	54.78
	LH (w/m ²)	72.21	69.57	132.71	103.20	89.45	116.00

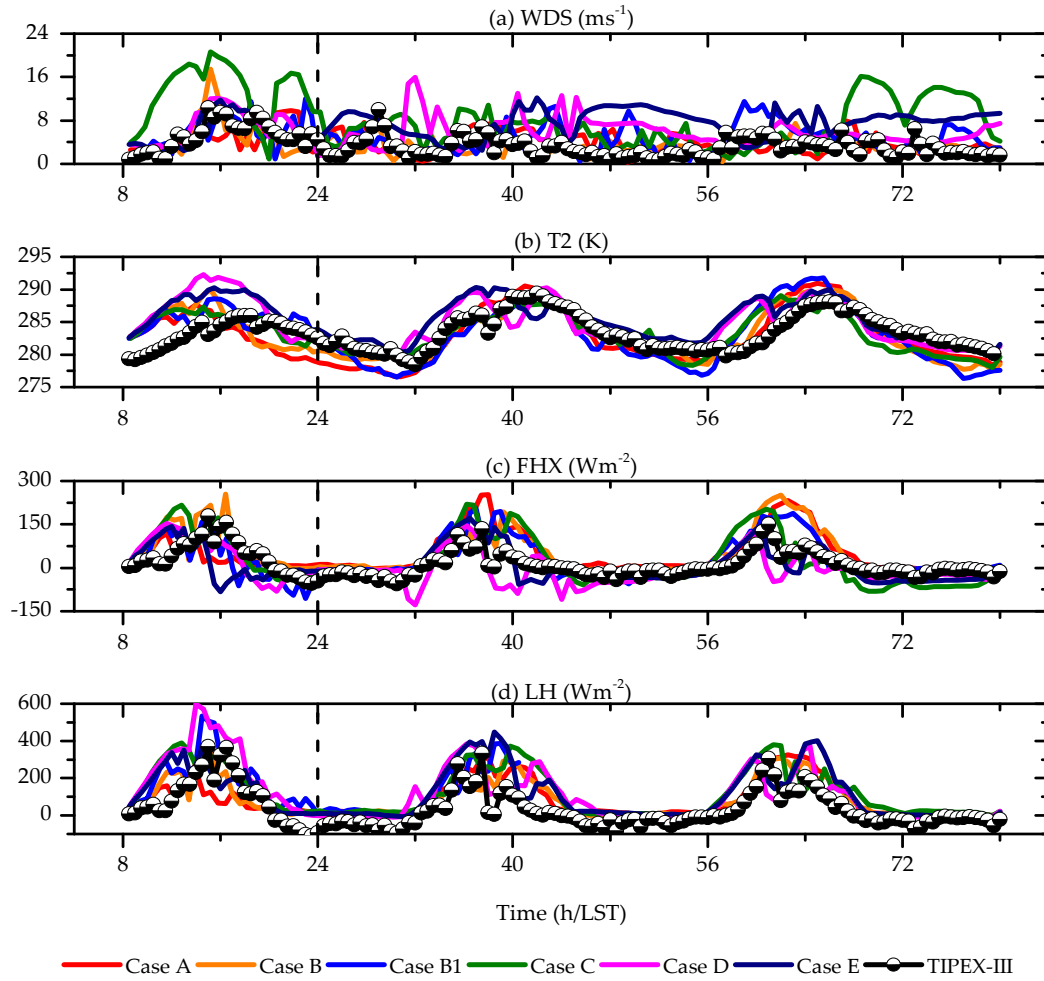


Figure 2: Time series of surface variables from $D0_{i=3}$ of the scenarios A, B and B1, and from $D0_{i=5}$ of the scenarios C, D and E (Table 4), compared to time series from Naqul (92.067, 31.483): (a) wind speed (WSD); (b) Two-meter temperature (T2); (c) the sensible heat flux (HFX) at the surface; (d) the latent heat flux (LH) at the surface. Dashed lines indicate the upper limit of spin-up time.

Overall, for surface meteorological variables and heat fluxes, considering the set of results in each scenario, scenarios B and D had more accurate and reliable results than scenarios A, B1, and C. However, compared to the scenario A we found that the observation nudging strategy improved WSD, FHX, and LH results in the scenario B and HFX results in the scenario C and D. In fact, some results from the scenario C such as MB relative to HFX and LH were least scores and have a relatively good RMSE. However, we believe that noise occurred while transitioning through the ‘ndown’ program during the performance of the one-way nesting strategy. This is because

3.2. The Simulated and Observed Boundary Layer Height

The ABL height is a fundamental parameter characterizing the depth of atmospheric mixing near the earth's surface. It is critical for understanding the cloud processes related to ABL features and their feedback on the weather and climate system. The detection of ABL height from Lidar is as follows: at the top of the ABL, water vapor decreases abruptly and affects the Lidar signal to change rapidly around the ABL top.

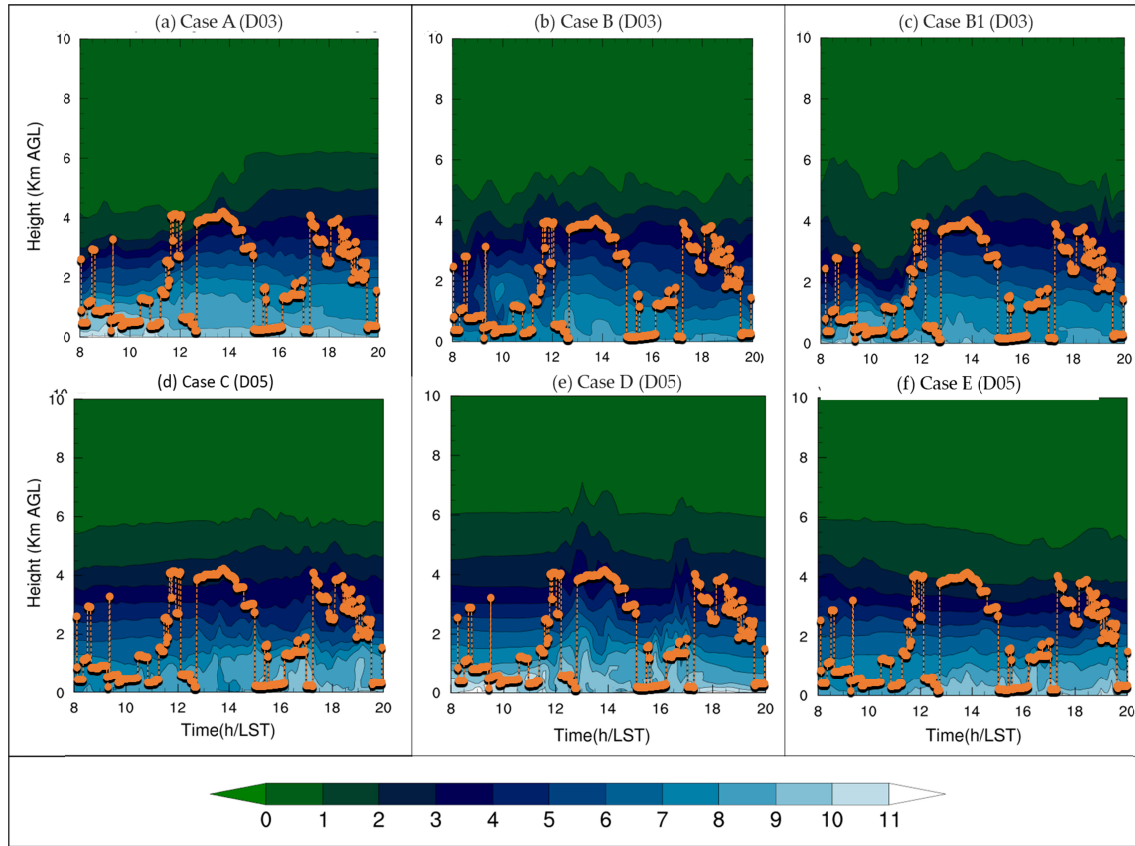


Figure 3: Time-high cross-section of water vapor mixing ratio (g/kg) (shaded) over Naqul predicted on July 19, 2014, at local standard time and compared to laser ceilometer measurements of the boundary layer height (ABL) from the Third Tibetan Plateau Atmospheric Science Experiment (TIPEX-III). Cases A, B and B_1 from $D0_{i=3} = D03$, C, D and E from $D0_{i=5} = D05$ represent scenarios in Table 4.

In this study, we compared the simulated ABL to that from the CL31 measurements based on the time-height cross-section of the water vapor mixing ratio. We found three peaks of the ABL from CL31 measurements, at 12:00, 14:00, and 18:00 LST. The peak found at 12:00 LST may be related to intermittent turbulence. The diurnal peak was reached around 14:00 LST. The peak found at 18:00 LST may have arisen from the high HFX released after intense convection developed in the early evening. We can also look for the last two peaks in the time series from temperature and heat fluxes shown in Figure 2 between the 56th and 72nd hours of the simulation period. The simulated ABL shows undulations and plumes of the water vapor mixing ratio with the mixing decreasing with height. We depicted the results of the comparison in Figure 3. Upon

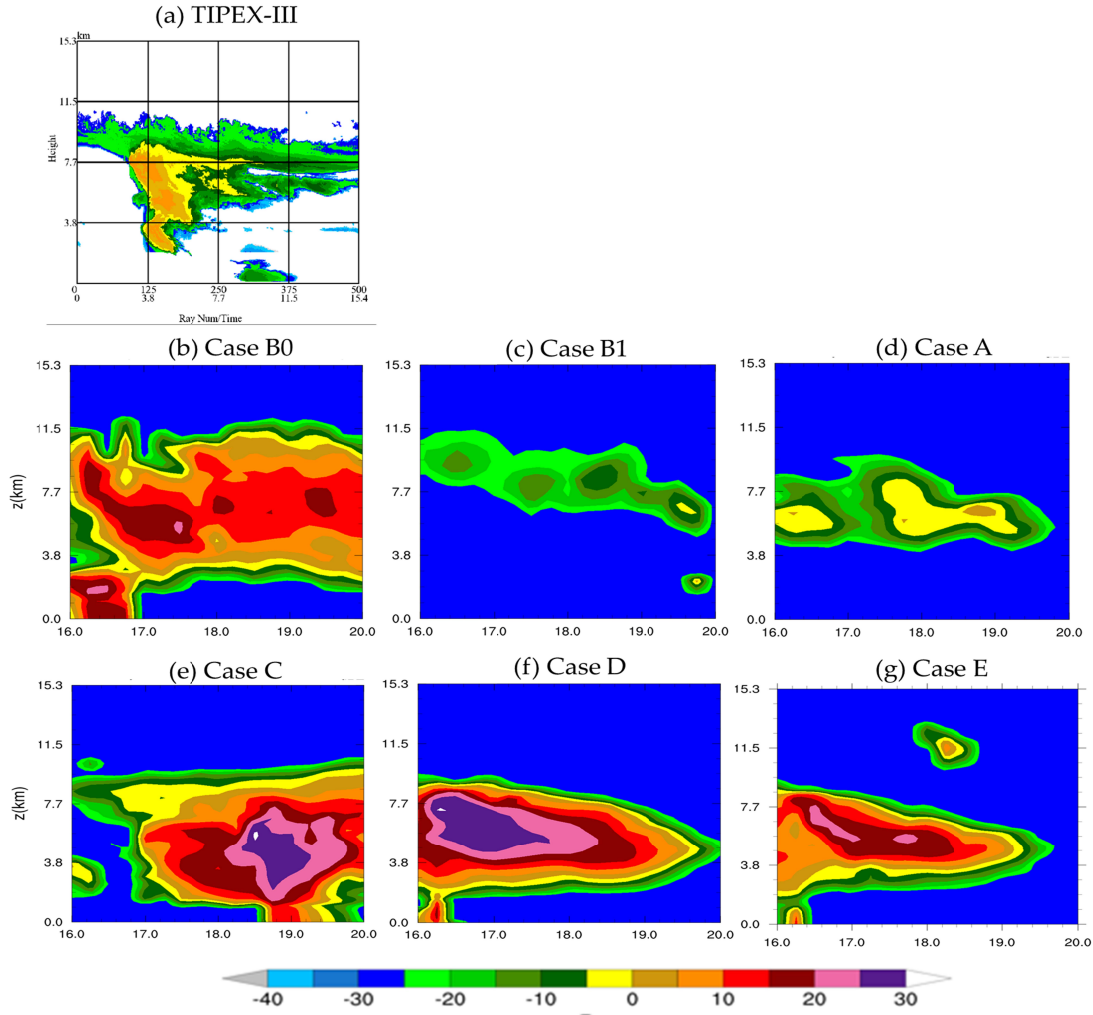
visual inspection, we can estimate the simulated ABL height as the height at which the water vapor mixing ratio is 4 g/kg. This is because the CL31 measurements fit better with that height in scenarios C and D (Figures 3d,e).

In the overall mesoscale simulation results, scenarios A, B, and B1 (Figures 3a,b,c) presented a convective ABL between 10:00 and 20:00 LST, slightly higher than the observed. We note that in dry and warm land surface-atmosphere conditions, the top of the ABL over TP is deep, while a shallow ABL characterizes the moist condition of the coupled system. Under current conditions, it is perceived that all mesoscale simulations will reproduce little clear skies with few cumulus clouds (examples: case B and B1 of Figures 5c,d). We note also that each of the scenarios A, B, B1 capture the observation field of the diurnal peak of the ABL. However, the model failed to reproduce clearly the ABL peak around 18:00 LST. This is probably related to the PBL scheme, which cannot treat the surface heterogeneity well. In scenarios C and D (Figures 3d,e), the ABL peaks collapsed slightly compared to the CL31 measurements, but the simulated ABL has a similar trend to CL31. The input from the mesoscale simulation forced LES from scenario C, which affected the simulated ABL structure. We can therefore consider that applying the one-way nesting strategy could increase the noise in the ABL structure due to complex topography that is not resolved in the scenario C. Particularly, in the scenario D (Figure 3d), the boundary between the free and moist atmospheric layers followed the trend of the CL31 measurement. Scenario E presented a relatively shallow ABL. According to our hypothesis, it is likely that scenario E will produce a cloudier sky. The ABL from each scenario, depending on its features, developed CC convection more or less consistent with the observed. To set this idea down, we discuss the convection that occurred between 16:00 and 20:00 LST in the next subsections.

3.3. Pattern Reflectivity and FY-2D Satellite Image

We compared the simulated reflectivity (Figures 4b,e) to the radar reflectivity from TIPEX-III performed over Naqu2 (Figure 4a). The maximum intensity of reflectivity in scenarios A and B1 was similar to the intensity (10 dBZ) of the observed reflectivity, whereas in scenarios B, C, D and E, the model overpredicted the intensity of the observed reflectivity by 30 dBZ. We verified from the observation that very weak or almost no precipitation occurred over Naqu2 between 15:04 and 18:46 LST. By contrast, the model presented maximum reflectivity before 18:00 LST in all scenarios except scenario C. Comparing the numerical pattern reflectivity in each scenario to the observed, the model anticipated the observed reflectivity over Naqu2 by at least three hours, which can be seen in the time series of surface variables shown earlier in Figure 3. The reflectivity in scenario C reflects the observed better than in other scenarios. The reflectivity in scenarios D and E (Figures 4f,g) reached a height above that observed in scenario C (Figure 4d) with similar intensity. But the maximum precipitation (the orange shaded reflectivity) observed from TIPE-III (Figure 4a) around 19:00 LST at the Naqu site was rather predicted just after 16:00 LST. The little improvement relative to the prediction time of the precipitation intensity in scenario C may be related to the combination of the one-way nesting and observation nudging strategies. Note that scenarios D and E have not applied a one-way nesting strategy. On the other hand, the earlier evaluation result showed that scenarios C, D and E overpredicted the surface wind speed and hence the latent heat flux and intense precipitation. Wind speed depends on the large-scale pressure gradient force and the local geography. In addition, as the wind speed is modulated by the large-scale forcing, it is obvious that scenarios D

524 and E presented different results from scenario C because they performed LES without a one-
 525 way nesting strategy. Furthermore, the difference between scenario D and E is because scenario
 526 E has not used observation nudging strategy.



527

528 **Figure 4:** Vertical cross-section of pattern reflectivity on day 3 of simulation period: (a) the
 529 observed radar reflectivity from TIPEX-III between 18:45 and 20:00 LST on July 19, 2014; (b–
 530 e) simulated reflectivity. Cases A, B and B1 from $D0_{i=3} = D03$, C, D and E from $D0_{i=5} = D05$
 531 represent scenarios in Table 4.

532 3.4. The Meso- and Micro-scales Liquid Water Content and The Vertical Wind Shear

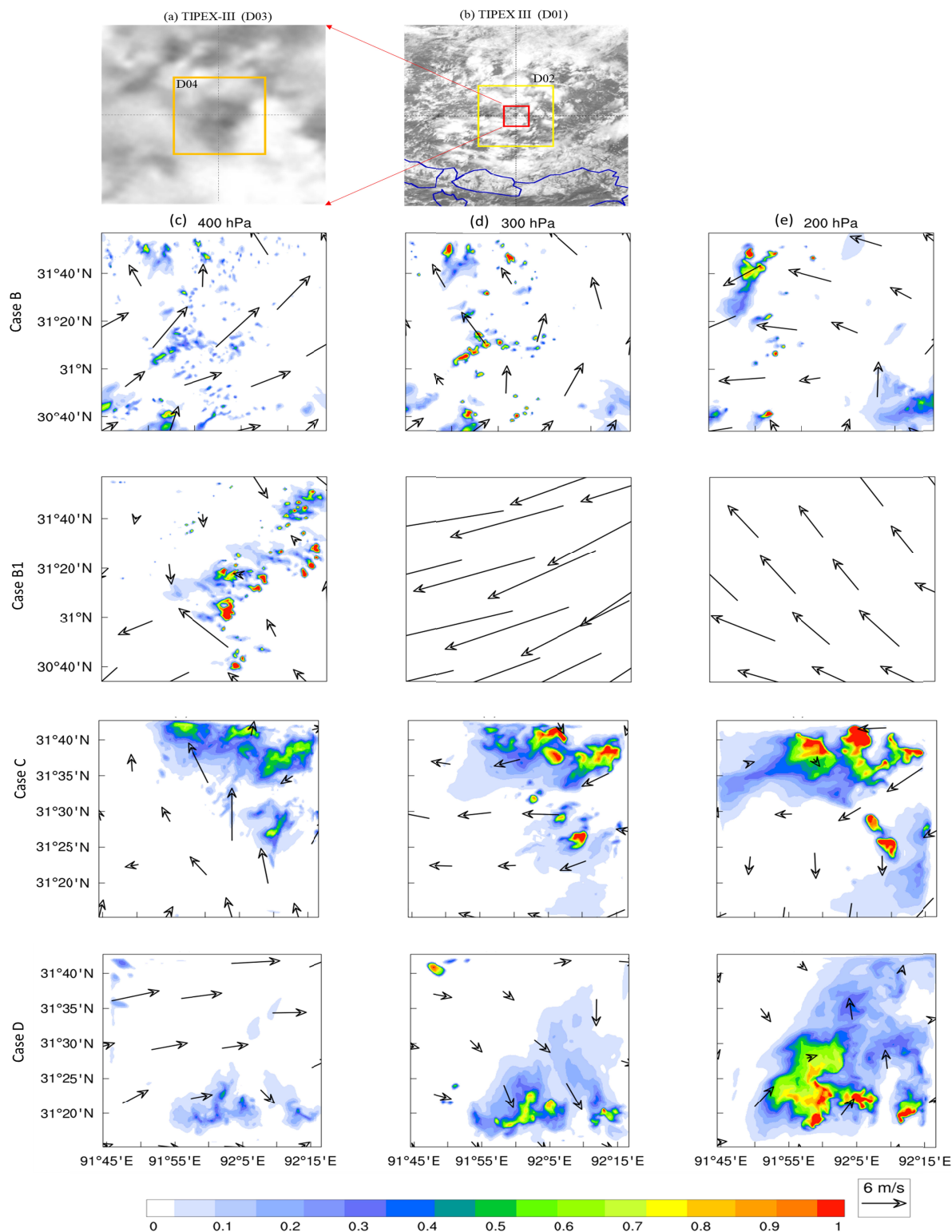
533 We investigated the types of CCs and the effect of the vertical wind shear on their
 534 development in each scenario, based on the amount of the liquid water content (LWC). Vertical
 535 wind shear is a factor that determines the origin of clouds forming over a given region, while the
 536 amount of LWC in the atmosphere determines what types of clouds form. We illustrated the
 537 LWC in Figure 5 at 200, 300 and 400 hPa levels, respectively, each overlapped with the vertical
 538 wind shear. Note that Fengyun's satellite images (Figures 5a,b) are plane projections including
 539 clouds from the low level to the tropopause. The white parts of Fengyun's satellite images

represent the CCs. The dark parts of the images represent no clouds. We depict LWC and wind shear at 16:48 LST. This analysis emphasizes CC and cumulonimbus clouds development. A study by Hess et al., (1998) classified the types of clouds associated with the amount of LWC over land and recommended $0.25 \text{ g/m}^3 \leq \text{LWC} \leq 0.3 \text{ g/m}^3$ for CC and stratocumulus clouds, and $1 \text{ g/m}^3 \leq \text{LWC} \leq 3 \text{ g/m}^3$ for cumulonimbus. Scenarios A and E were useless in this analysis due to their uncertainty with the observed clouds. Moreover, these scenarios were not the target scenarios so far.

In scenario, B, Figures 5c,d shows a spatial distribution of LWC similar to that of the cloud distribution in Fengyun's satellite image (Figure 5a). However, compared to the satellite image, scenario B shows scattered small CCs and some Cumulonimbus with $\text{LWC} \geq 1 \text{ g/m}^3$ from the mid-level (Figure 5d) to the upper level (Figure 5e) at the northwest and southeast flanks, respectively. Scenario B also presents a strong vertical wind shear. As we can see in Figure 5c, there is a southwesterly low-level jet (LLJ) at 400hPa. The LLJ is a monsoonal wind that provides moist air favorable for cloud formation. The southeasterly wind dominates the middle-level (300 hPa). The upper-level (200 hPa) is dominated by the easterly wind with strong horizontal wind shear. We can also see at 200 hPa level that the southeast wind is abruptly deflected west by the northeast wind.

Scenario B1 presents an intense mesoscale convective system at the 400 hPa level (Figure 5c), but subsidence dominates at 300 hPa levels. In the mesoscale convective system, Figure 5c of scenario B1 shows favorable conditions ($\text{LWC} > 1 \text{ g/m}^3$) for cumulonimbus clouds. However, the subsidence limits the cumulonimbus to expand vertically due to a strong northwesterly upper-level jet (ULJ). In this sense, the large-scale forcing played an important role in cumulus development on July 19, 2014. Indeed, in scenario B1, we have emphasized external forcing by increasing the number of model levels in the ABL, but the results are not consistent with the observation.

The scenario C presents the results of LES with one-way nesting from $D0_{i=4}$. This scenario has developed cumulonimbus with $\text{LWC} \geq 1 \text{ g/m}^3$ and has a spatial distribution of the LWC (Figure 5e) similar to the observed clouds (Figure 5a). Noted that this scenario presented the ABL water vapor relatively consistent with the observation. Scenario C predicted low and upper-level wind differently from scenario B. There is southeasterly wind at 400 hPa level (Figure 5c), easterly wind at 300 hPa level (Figure 5d), and northeasterly wind that predominates at the 200 hPa level. This study assumes that the wind field in scenario C from 200 to 400 hPa levels is more consistent with the observed than in scenario B because scenario C presented better clouds pattern than scenario B. Thus, the biased surface wind from scenario C discussed in section 3.1) did not influence the spatial distribution of the LWC. This is true when referring to the results from scenario B1, meaning that the internal forcing dominated the CC development on July 19, 2014 at the Naqu site.



580

581 **Figure 5:** Liquid water content (LWC) and vertical wind shear at 16:48 local standard time
 582 (LST); vector field stands for wind direction and shaded represents LWC (g/m^3). Classification
 583 clouds types associated with the amount of LWC can be found in (Hess et al., 1998). Cases B
 584 and B1 from $D0_{i=3} = D03$, and C and D from $D0_{i=4} = D04$ represent the scenarios in Table 4.

The scenario D (Figures 5d,e), LES without a one-way nesting strategy presents cumulonimbus clouds from $D0_{i=4}$ with $LWC \geq 1 \text{ g/m}^3$. The atmosphere was quite turbulent due to pronounced wind shear. For example, the west wind at the 400 hPa level (Figure 5d) changed to a north wind at the 300 hPa level. By contrast, the wind at the 200 hPa level (Figure 5e) has no specific direction. We note that scenario D has the best distribution of the water vapor mixing ratio in the ABL. When compared to scenarios B, B1, and C, scenario D was able to handle a complex orography. However, this scenario failed to reproduce the observed clouds.

4. Summary and Conclusions

We explored the ability of the combined weather research and forecasting large-eddy simulation (WRF-LES) in the simulation of the atmospheric boundary-layer (ABL) processes of cumulus clouds (CCs) development over the south Tibetan plateau (STP). The goal of this study was to increase our understanding of the WRF-LES's ability to predict the ABL processes of CCs development over the complex orography, which is an unresolved problem in numerical modeling. We carried out simulations of six scenarios with different setups and compared the results to observations from the third Tibetan Plateau Atmospheric Science Experiment (TIPEX-III), including Lidar ceilometer measurements, Fengyun 2D satellite images, radar reflectivity, sounding, and surface-base measurements such as temperature, wind, and heat fluxes. The new findings were obtained by applying observation nudging strategies and one-way nesting in two separate iterations.

Six scenarios, with mesoscale simulation, runs in scenarios A, B and B1, and large-eddy simulation (LES) runs in scenarios C, D and E, are discussed. Scenarios A and E were benchmark experiments to help determine the optimality of observation nudging used in scenarios B and D, respectively. We applied observation nudging in scenarios the B, B1, C, and D. scenario B determined the impact of observation nudging on the simulation results. Scenario C determined the effect of large-scale forcing on microscale circulation. Scenario C differed from scenario D only in the use of the one-way nesting strategy, while scenario D was a control experiment to help determine the optimality of the one-way nesting strategy used in scenario C.

Among the six scenarios carried out, the model setting with observations nudging yielded better results than those without nudging. Compared to the observations, the control scenarios A, B1 and E do not well reflect the field's observations. Scenario B1, which emphasized an external forcing, did not yield consistent results with the observations. As a result, large-scale forcing played an important role in CCs development over TP. The evaluation results on one hand also showed that scenario B perfectly reproduced the surface variables nevertheless with low microphysical particles while on the other hand scenario D reproduced an ABL, which is consistent with the observations however this scenario could not correctly reproduce the microphysics patterns. The scenario C had a relatively good representation of ABL and better reproduced the microphysical pattern, which also confirms the role of the large-scale forcing in cumulus development over STP.

For CC simulations, we recommend scenarios B and C, which generally captured the overall joint effects of ABL processes and cumulus cloud development, observed on July 19, 2014. However, the WRF-LES presented some biases since the reliable data are still insufficient such as sounding that take place twice a day, which is a very low temporal frequency. Therefore,

we suggest that for a scientific purpose and clouds simulation over STP, scenarios B and C can still be improved, by focusing on the model's response to the terrain and meteorological initial and boundary conditions. There is an interest in statistically stabilizing the model on the spin-up because the coupled WRF-LES would require the mesoscale simulation data to be reliable. In this case, this study performed a series of simulations by varying the spin-up time as preliminary work to determine the time interval that best matched this simulation. Based on these results, part B of this paper will discuss the development mechanism of the deep cumulus convection over STP on July 19, 2014.

Acknowledgment:

The authors would like to thank the Tianhe for providing a high-performance computing (HPC) system for this work. The first author thanks Hu Wenhao and Zhang Tianyu for helping to solve the technical issues encountered during this work. He would like also to thank Professor Banna Magolmeena at the University of Lomé in Togo for his particular attention to the author's Ph.D. studies. He wishes to express his gratitude to the WMO and the National Meteorological Authority of Togo for making him a meteorologist.

This work was supported by the Chinese academy of sciences (CAS), the world academy of sciences (TWAS) and substantially supported by the National Science and Technology Major Project of the Ministry of Science and Technology of China (2018YFC1505704).

References

- Anthes, R. A. (1986). The General Question of Predictability. In P. S. Ray (Ed.), *Mesoscale Meteorology and Forecasting* (pp. 636–656). Boston, MA: American Meteorological Society. https://doi.org/10.1007/978-1-935704-20-1_27
- Ao, Y., Li, J., Li, Z., Lyu, S., Jiang, C., & Wang, M. (2017). Relation between the Atmospheric Boundary Layer and Impact Factors under Severe Surface Thermal Conditions. *Advances in Meteorology*, 2017, e8352461. <https://doi.org/10.1155/2017/8352461>
- Arya, S. P. (Ed.). (2001). Chapter 1 Introduction. In *International Geophysics* (Vol. 79, pp. 1–10). Academic Press. [https://doi.org/10.1016/S0074-6142\(01\)80017-6](https://doi.org/10.1016/S0074-6142(01)80017-6)
- Betts, A. K., & Ball, J. H. (1994). Budget analysis of FIFE 1987 sonde data. *Journal of Geophysical Research: Atmospheres*, 99(D2), 3655–3666. <https://doi.org/10.1029/93JD02739>

- Canuto, V. M., & Cheng, Y. (1997). Determination of the Smagorinsky–Lilly constant CS. *Physics of Fluids*, 9(5), 1368–1378. <https://doi.org/10.1063/1.869251>
- Chen, Henderson-Sellers, A., Milly, P. C. D., Pitman, A. J., Beljaars, A. C. M., Polcher, J., et al. (1997). Cabauw Experimental Results from the Project for Intercomparison of Land-Surface Parameterization Schemes. *Journal of Climate*, 10(6), 1194–1215. [https://doi.org/10.1175/1520-0442\(1997\)010<1194:CERFTP>2.0.CO;2](https://doi.org/10.1175/1520-0442(1997)010<1194:CERFTP>2.0.CO;2)
- Chen, X., Añel, J. A., Su, Z., Torre, L. de la, Kelder, H., Peet, J. van, & Ma, Y. (2013). The Deep Atmospheric Boundary Layer and Its Significance to the Stratosphere and Troposphere Exchange over the Tibetan Plateau. *PLOS ONE*, 8(2), e56909. <https://doi.org/10.1371/journal.pone.0056909>
- Chen, X., Škerlak, B., Rotach, M. W., Añel, J. A., Su, Z., Ma, Y., & Li, M. (2016). Reasons for the Extremely High-Ranging Planetary Boundary Layer over the Western Tibetan Plateau in Winter. *Journal of the Atmospheric Sciences*, 73(5), 2021–2038. <https://doi.org/10.1175/JAS-D-15-0148.1>
- Cheng, W.-C., Kendall, D. R., Putti, M., & Yeh, W. W.-G. (2009). A nudging data assimilation algorithm for the identification of groundwater pumping. *Water Resources Research*, 45(8). <https://doi.org/10.1029/2008WR007602>
- Chow, F. K., & Street, R. L. (2009). Evaluation of Turbulence Closure Models for Large-Eddy Simulation over Complex Terrain: Flow over Askervein Hill. *Journal of Applied Meteorology and Climatology*, 48(5), 1050–1065. <https://doi.org/10.1175/2008JAMC1862.1>
- Chow, F. K., Street, R. L., Xue, M., & Ferziger, J. H. (2005). Explicit Filtering and Reconstruction Turbulence Modeling for Large-Eddy Simulation of Neutral Boundary

- Layer Flow. *Journal of the Atmospheric Sciences*, 62(7), 2058–2077.
<https://doi.org/10.1175/JAS3456.1>
- Cotton, W. R., & Anthes, R. A. (Eds.). (1992). Chapter 8 Cumulus Clouds. In *International Geophysics* (Vol. 44, pp. 368–454). Academic Press. [https://doi.org/10.1016/S0074-6142\(08\)60547-1](https://doi.org/10.1016/S0074-6142(08)60547-1)
- Couvreux, F., Guichard, F., Austin, P. H., & Chen, F. (2009). Nature of the Mesoscale Boundary Layer Height and Water Vapor Variability Observed 14 June 2002 during the IHOP_2002 Campaign. *Monthly Weather Review*, 137(1), 414–432.
<https://doi.org/10.1175/2008MWR2367.1>
- Dai, C., Wang, Q., Kalogiros, J. A., Lenschow, D. H., Gao, Z., & Zhou, M. (2014). Determining Boundary-Layer Height from Aircraft Measurements. *Boundary-Layer Meteorology*, 152(3), 277–302. <https://doi.org/10.1007/s10546-014-9929-z>
- Deardorff, J. W. (1980). Stratocumulus-capped mixed layers derived from a three-dimensional model. *Boundary-Layer Meteorology*, 18(4), 495–527.
<https://doi.org/10.1007/BF00119502>
- Ding, J., Cuo, L., Zhang, Y., & Zhu, F. (2018). Monthly and annual temperature extremes and their changes on the Tibetan Plateau and its surroundings during 1963–2015. *Scientific Reports*, 8(1), 11860. <https://doi.org/10.1038/s41598-018-30320-0>
- Dudhia, J. (2014). A history of mesoscale model development. *Asia-Pacific Journal of Atmospheric Sciences*, 50(1), 121–131. <https://doi.org/10.1007/s13143-014-0031-8>
- Emanuel, K. A. (Ed.). (1993). *The Representation of Cumulus Convection in Numerical Models*. American Meteorological Society. <https://doi.org/10.1007/978-1-935704-13-3>

- Emanuel, K. A. (1997). Overview of Atmospheric Convection. In R. K. Smith (Ed.), *The Physics and Parameterization of Moist Atmospheric Convection* (pp. 1–28). Dordrecht: Springer Netherlands. https://doi.org/10.1007/978-94-015-8828-7_1
- Flohn, H. (1968). *Contributions to a meteorology of the Tibetan highlands*. Fort Collins, Colo. : Department of Atmospheric Science, Colorado State University, 1968., U.S.A. Retrieved from <https://fmpl.catalog.aspcat.info/ColoGovDoc/ocn719384850>
- Fu, R., Hu, Y., Wright, J. S., Jiang, J. H., Dickinson, R. E., Chen, M., et al. (2006). Short circuit of water vapor and polluted air to the global stratosphere by convective transport over the Tibetan Plateau. *Proceedings of the National Academy of Sciences*, 103(15), 5664–5669. <https://doi.org/10.1073/pnas.0601584103>
- Fu, Y., Ma, Y., Zhong, L., Yang, Y., Guo, X., Wang, C., et al. (2020). Land-surface processes and summer-cloud-precipitation characteristics in the Tibetan Plateau and their effects on downstream weather: a review and perspective. *National Science Review*, 7(3), 500–515. <https://doi.org/10.1093/nsr/nwz226>
- Fujita, T. T. (1986). Mesoscale Classifications: Their History and Their Application to Forecasting. In P. S. Ray (Ed.), *Mesoscale Meteorology and Forecasting* (pp. 18–35). Boston, MA: American Meteorological Society. https://doi.org/10.1007/978-1-935704-20-1_2
- Gao, W., Sui, C.-H., Fan, J., Hu, Z., & Zhong, L. (2016). A study of cloud microphysics and precipitation over the Tibetan Plateau by radar observations and cloud-resolving model simulations: Cloud Microphysics over Tibetan Plateau. *Journal of Geophysical Research: Atmospheres*, 121(22), 13,735–13,752. <https://doi.org/10.1002/2015JD024196>

- 724 Gavilán, P., & Berengena, J. (2006). Accuracy of the Bowen ratio-energy balance method for
725 measuring latent heat flux in a semiarid advective environment. *Irrigation Science*, 25(2),
726 127–140. <https://doi.org/10.1007/s00271-006-0040-1>
- 727 Gentry, M. S., & Lackmann, G. M. (2010). Sensitivity of Simulated Tropical Cyclone Structure
728 and Intensity to Horizontal Resolution. *Monthly Weather Review*, 138(3), 688–704.
729 <https://doi.org/10.1175/2009MWR2976.1>
- 730 Heinze, R., Moseley, C., Böske, L. N., Muppa, S. K., Maurer, V., Raasch, S., & Stevens, B.
731 (2017). Evaluation of large-eddy simulations forced with mesoscale model output for a
732 multi-week period during a measurement campaign. *Atmospheric Chemistry and Physics*,
733 17(11), 7083–7109. <https://doi.org/10.5194/acp-17-7083-2017>
- 734 Hess, M., Koepke, P., & Schult, I. (1998). Optical Properties of Aerosols and Clouds: The
735 Software Package OPAC. *Bulletin of the American Meteorological Society*, 79(5), 831–
736 844. [https://doi.org/10.1175/1520-0477\(1998\)079<0831:OPOAAC>2.0.CO;2](https://doi.org/10.1175/1520-0477(1998)079<0831:OPOAAC>2.0.CO;2)
- 737 van den Hurk, B. J. J. M., & Holtslag, A. A. M. (1997). On the bulk parameterization of surface
738 fluxes for various conditions and parameter ranges. *Boundary-Layer Meteorology*, 82(1),
739 119–133. <https://doi.org/10.1023/A:1000245600901>
- 740 Iacono, M. J., Delamere, J. S., Mlawer, E. J., Shephard, M. W., Clough, S. A., & Collins, W. D.
741 (2008). Radiative forcing by long-lived greenhouse gases: Calculations with the AER
742 radiative transfer models. *Journal of Geophysical Research*, 113(D13), D13103.
743 <https://doi.org/10.1029/2008JD009944>
- 744 IPCC, I. P. on C. C. (2014). *Climate Change 2013 - The Physical Science Basis: Working Group*
745 *I Contribution to the Fifth Assessment Report of the Intergovernmental Panel on Climate*

- Change. Cambridge: Cambridge University Press.
<https://doi.org/10.1017/CBO9781107415324>
- Janjic, Z. (2002). Nonsingular Implementation of the Mellor–Yamada Level 2.5 Scheme in the NCEP Meso Model. *NCEP Office Note*, 436.
- Jeworrek, J., West, G., & Stull, R. (2019). Evaluation of Cumulus and Microphysics Parameterizations in WRF across the Convective Gray Zone. *Weather and Forecasting*, 34(4), 1097–1115. <https://doi.org/10.1175/WAF-D-18-0178.1>
- Jiménez, P. A., Dudhia, J., González-Rouco, J. F., Navarro, J., Montávez, J. P., & García-Bustamante, E. (2012). A Revised Scheme for the WRF Surface Layer Formulation. *Monthly Weather Review*, 140(3), 898–918. <https://doi.org/10.1175/MWR-D-11-00056.1>
- Kain, J. S. (2004). The Kain–Fritsch Convective Parameterization: An Update. *Journal of Applied Meteorology and Climatology*, 43(1), 170–181. [https://doi.org/10.1175/1520-0450\(2004\)043<0170:TKCPAU>2.0.CO;2](https://doi.org/10.1175/1520-0450(2004)043<0170:TKCPAU>2.0.CO;2)
- Kane, R. L., & Klein, D. E. (2005). Carbon Sequestration. In L. K. Wang, N. C. Pereira, & Y.-T. Hung (Eds.), *Advanced Air and Noise Pollution Control* (pp. 97–112). Totowa, NJ: Humana Press. https://doi.org/10.1007/978-1-59259-779-6_3
- Kotthaus, S., & Grimmond, C. S. B. (2018). Atmospheric boundary-layer characteristics from ceilometer measurements. Part 1: A new method to track mixed layer height and classify clouds. *Quarterly Journal of the Royal Meteorological Society*, 144(714), 1525–1538. <https://doi.org/10.1002/qj.3299>
- Krueger, S. K. (1988). Numerical Simulation of Tropical Cumulus Clouds and Their Interaction with the Subcloud Layer. *Journal of the Atmospheric Sciences*, 45(16), 2221–2250. [https://doi.org/10.1175/1520-0469\(1988\)045<2221:NSOTCC>2.0.CO;2](https://doi.org/10.1175/1520-0469(1988)045<2221:NSOTCC>2.0.CO;2)

- 769 Larson, K., Hartmann, D. L., & Klein, S. A. (1999). The Role of Clouds, Water Vapor,
770 Circulation, and Boundary Layer Structure in the Sensitivity of the Tropical Climate.
771 *Journal of Climate*, 12(8), 2359–2374. [https://doi.org/10.1175/1520-](https://doi.org/10.1175/1520-0442(1999)012<2359:TROCWV>2.0.CO;2)
772 0442(1999)012<2359:TROCWV>2.0.CO;2
- 773 Lei, Y., Shi, J., Xiong, C., & Ji, D. (2021). Tracking the Atmospheric–Terrestrial Water Cycle
774 over the Tibetan Plateau Based on ERA5 and GRACE. *Journal of Climate*, 34(15), 6459–
775 6471. <https://doi.org/10.1175/JCLI-D-20-0692.1>
- 776 Li, G., Tingyang, D., Jun, W., Yuanfa, G., Haginoya, S., Longxun, C., & Weiliang, L. (1996).
777 Determination of the Drag Coefficient over the Tibetan Plateau. *Advances in Atmospheric*
778 *Sciences*, 13(4), 511–518. <https://doi.org/10.1007/BF03342041>
- 779 Li, L., Yang, S., Wang, Z., Zhu, X., & Tang, H. (2010). Evidence of Warming and Wetting
780 Climate over the Qinghai-Tibet Plateau. *Arctic, Antarctic, and Alpine Research*, 42(4),
781 449–457. <https://doi.org/10.1657/1938-4246-42.4.449>
- 782 Li, Y., & Gao, W. (2007). Atmospheric Boundary Layer Circulation on the Eastern Edge of the
783 Tibetan Plateau, China, in Summer. *Arctic, Antarctic, and Alpine Research*, 39(4), 708–
784 713. [https://doi.org/10.1657/1523-0430\(07-504\)\[LI\]2.0.CO;2](https://doi.org/10.1657/1523-0430(07-504)[LI]2.0.CO;2)
- 785 Liu, L., Zheng, J., Ruan, Z., Cui, Z., Hu, Z., Wu, S., et al. (2015). Comprehensive radar
786 observations of clouds and precipitation over the Tibetan Plateau and preliminary
787 analysis of cloud properties. *Journal of Meteorological Research*, 29(4), 546–561.
788 <https://doi.org/10.1007/s13351-015-4208-6>
- 789 Liu, X., Yin, Z.-Y., Shao, X., & Qin, N. (2006). Temporal trends and variability of daily
790 maximum and minimum, extreme temperature events, and growing season length over

- the eastern and central Tibetan Plateau during 1961–2003. *Journal of Geophysical Research: Atmospheres*, 111(D19). <https://doi.org/10.1029/2005JD006915>
- Liu, Y., Warner, T., Liu, Y., Vincent, C., Wu, W., Mahoney, B., et al. (2011). Simultaneous nested modeling from the synoptic scale to the LES scale for wind energy applications. *Journal of Wind Engineering and Industrial Aerodynamics*, 99(4), 308–319. <https://doi.org/10.1016/j.jweia.2011.01.013>
- Liu, Y., Muñoz-Esparza, D., Hu, F., Yan, C., & Miao, S. (2020). Simulation of Flow Fields in Complex Terrain with WRF-LES: Sensitivity Assessment of Different PBL Treatments. *Journal of Applied Meteorology and Climatology*, 59(9), 1481–1501. <https://doi.org/10.1175/JAMC-D-19-0304.1>
- Luo, Y., Zhang, R., Qian, W., Luo, Z., & Hu, X. (2011). Intercomparison of Deep Convection over the Tibetan Plateau–Asian Monsoon Region and Subtropical North America in Boreal Summer Using CloudSat/CALIPSO Data. *Journal of Climate*, 24(8), 2164–2177. <https://doi.org/10.1175/2010JCLI4032.1>
- Margulis, S. A., & Entekhabi, D. (2004). Boundary-Layer Entrainment Estimation Through Assimilation of Radiosonde and Micrometeorological Data into a Mixed-Layer Model. *Boundary-Layer Meteorology*, 110(3), 405–433. <https://doi.org/10.1023/B:BOUN.0000007221.53446.46>
- Mechem, D. B., & Oberthaler, A. J. (2013). Numerical simulation of tropical cumulus congestus during TOGA COARE. *Journal of Advances in Modeling Earth Systems*, 5(3), 623–637. <https://doi.org/10.1002/jame.20043>
- Mirocha, J. D., Lundquist, J. K., & Kosović, B. (2010). Implementation of a Nonlinear Subfilter Turbulence Stress Model for Large-Eddy Simulation in the Advanced Research WRF

- Model. *Monthly Weather Review*, 138(11), 4212–4228.
<https://doi.org/10.1175/2010MWR3286.1>
- Mlawer, E. J., Taubman, S. J., Brown, P. D., Iacono, M. J., & Clough, S. A. (1997). Radiative transfer for inhomogeneous atmospheres: RRTM, a validated correlated-k model for the longwave. *Journal of Geophysical Research: Atmospheres*, 102(D14), 16663–16682.
<https://doi.org/10.1029/97JD00237>
- Moeng, C.-H., & Wyngaard, J. C. (1989). Evaluation of Turbulent Transport and Dissipation Closures in Second-Order Modeling. *Journal of the Atmospheric Sciences*, 46(14), 2311–2330. [https://doi.org/10.1175/1520-0469\(1989\)046<2311:EOTTAD>2.0.CO;2](https://doi.org/10.1175/1520-0469(1989)046<2311:EOTTAD>2.0.CO;2)
- Niu, G.-Y., Yang, Z.-L., Mitchell, K. E., Chen, F., Ek, M. B., Barlage, M., et al. (2011). The community Noah land surface model with multiparameterization options (Noah-MP): 1. Model description and evaluation with local-scale measurements. *Journal of Geophysical Research*, 116(D12), D12109. <https://doi.org/10.1029/2010JD015139>
- Powers, J. G., Klemp, J. B., Skamarock, W. C., Davis, C. A., Dudhia, J., Gill, D. O., et al. (2017). The Weather Research and Forecasting Model: Overview, System Efforts, and Future Directions. *Bulletin of the American Meteorological Society*, 98(8), 1717–1737.
<https://doi.org/10.1175/BAMS-D-15-00308.1>
- Ravichandran, S., & Narasimha, R. (2020). Non-Precipitating Shallow Cumulus Clouds: Theory and Direct Numerical Simulation. *ArXiv:2004.09631 [Physics]*. Retrieved from <http://arxiv.org/abs/2004.09631>
- Ray, P. (2015). *Mesoscale Meteorology and Forecasting*. Springer.

- Reen, B. P., Dumais, R. E., & Passner, J. E. (2016). Mitigating Excessive Drying from the Use of Observations in Mesoscale Modeling. *Journal of Applied Meteorology and Climatology*, 55(2), 365–388. <https://doi.org/10.1175/JAMC-D-14-0301.1>
- Sato, T. (2009). Influences of subtropical jet and Tibetan Plateau on precipitation pattern in Asia: Insights from regional climate modeling. *Quaternary International*, 194(1–2), 148–158. <https://doi.org/10.1016/j.quaint.2008.07.008>
- Sertel, E., Robock, A., & Ormeci, C. (2010). Impacts of land cover data quality on regional climate simulations. *International Journal of Climatology*, 30(13), 1942–1953. <https://doi.org/10.1002/joc.2036>
- Shin, H. H., & Dudhia, J. (2016). Evaluation of PBL Parameterizations in WRF at Subkilometer Grid Spacings: Turbulence Statistics in the Dry Convective Boundary Layer. *Monthly Weather Review*, 144(3), 1161–1177. <https://doi.org/10.1175/MWR-D-15-0208.1>
- Skamarock, W., Klemp, J., Dudhia, J., Gill, D., Barker, D., Wang, W., et al. (2008). *A Description of the Advanced Research WRF Version 3* [Application/pdf] (p. 1002 KB). UCAR/NCAR. <https://doi.org/10.5065/D68S4MVH>
- Slättberg, N., & Chen, D. (2020). *A long-term Climatology of Planetary Boundary Layer Height over the Tibetan Plateau revealed by ERA5* (No. EGU2020-5517). Presented at the EGU2020, Copernicus Meetings. <https://doi.org/10.5194/egusphere-egu2020-5517>
- Sokół, P., Stachlewska, I. S., Ungureanu, I., & Stefan, S. (2014). Evaluation of the boundary layer morning transition using the CL-31 ceilometer signals. *Acta Geophysica*, 62(2), 367–380. <https://doi.org/10.2478/s11600-013-0158-5>
- Soriano, C., Jorba, O., & Baldasano, J. M. (2004). One-Way Nesting Versus Two-Way Nesting: Does It Really Make a Difference? In C. Borrego & G. Schayes (Eds.), *Air Pollution*

- 858 *Modeling and Its Application XV* (pp. 177–185). Boston: Kluwer Academic Publishers.
859 https://doi.org/10.1007/0-306-47813-7_18
- 860 Stanski, H. R., Wilson, L. J., Burrows, W. R., & Organization (WMO), W. M. (1989). *WWW*
861 *Technical report, 08. Survey of common verification methods in meteorology*. Geneva:
862 WMO.
- 863 Takemi, T., & Rotunno, R. (2003). The Effects of Subgrid Model Mixing and Numerical
864 Filtering in Simulations of Mesoscale Cloud Systems. *Monthly Weather Review*, 131(9),
865 2085–2101. [https://doi.org/10.1175/1520-0493\(2003\)131<2085:TEOSMM>2.0.CO;2](https://doi.org/10.1175/1520-0493(2003)131<2085:TEOSMM>2.0.CO;2)
- 866 Talbot, C., Bou-Zeid, E., & Smith, J. (2012). Nested Mesoscale Large-Eddy Simulations with
867 WRF: Performance in Real Test Cases. *Journal of Hydrometeorology*, 13(5), 1421–1441.
868 <https://doi.org/10.1175/JHM-D-11-048.1>
- 869 Tingyang, D., & Reiter, E. R. (1990). Some characteristics of cumulus convection over the
870 Tibetan Plateau. *Advances in Atmospheric Sciences*, 7(1), 87–97.
871 <https://doi.org/10.1007/BF02919171>
- 872 Verma, S. B., Baldocchi, D. D., Anderson, D. E., Matt, D. R., & Clement, R. J. (1986). Eddy
873 fluxes of CO₂, water vapor, and sensible heat over a deciduous forest. *Boundary-Layer*
874 *Meteorology*, 36(1–2), 71–91. <https://doi.org/10.1007/BF00117459>
- 875 Wang, J., Chen, X., Hu, Q., & Liu, J. (2020). Responses of Terrestrial Water Storage to Climate
876 Variation in the Tibetan Plateau. *Journal of Hydrology*, 584, 124652.
877 <https://doi.org/10.1016/j.jhydrol.2020.124652>
- 878 Wang, T., Hu, C., Li, N., & Hou, Z. (2002). Numerical analysis of ground temperature in
879 Qinghai-Tibet Plateau. *Science in China Series E: Technological Science*, 45(4), 433–443.
880 <https://doi.org/10.1360/02ye9050>

- Willmott, C. J., Ackleson, S. G., Davis, R. E., Feddema, J. J., Klink, K. M., Legates, D. R., et al. (1985). Statistics for the evaluation and comparison of models. *Journal of Geophysical Research: Oceans*, 90(C5), 8995–9005. <https://doi.org/10.1029/JC090iC05p08995>
- Wu, G., Liu, Y., Zhang, Q., Duan, A., Wang, T., Wan, R., et al. (2007). The Influence of Mechanical and Thermal Forcing by the Tibetan Plateau on Asian Climate. *Journal of Hydrometeorology*, 8(4), 770–789. <https://doi.org/10.1175/JHM609.1>
- Yanai, M., & Li, C. (1994). Mechanism of Heating and the Boundary Layer over the Tibetan Plateau. *Monthly Weather Review*, 122(2), 305–323. [https://doi.org/10.1175/1520-0493\(1994\)122<0305:MOHATB>2.0.CO;2](https://doi.org/10.1175/1520-0493(1994)122<0305:MOHATB>2.0.CO;2)
- Yang, K., Koike, T., Fujii, H., Tamura, T., Xu, X., Bian, L., & Zhou, M. (2004). The Daytime Evolution of the Atmospheric Boundary Layer and Convection over the Tibetan Plateau: Observations and Simulations. *Journal of the Meteorological Society of Japan*, 82(6), 1777–1792. <https://doi.org/10.2151/jmsj.82.1777>
- Yang, Z.-L., Niu, G.-Y., Mitchell, K. E., Chen, F., Ek, M. B., Barlage, M., et al. (2011). The community Noah land surface model with multiparameterization options (Noah-MP): 2. Evaluation over global river basins. *Journal of Geophysical Research*, 116(D12), D12110. <https://doi.org/10.1029/2010JD015140>
- Yesubabu, V., Srinivas, C. V., Ramakrishna, S. S. V. S., & Hari Prasad, K. B. R. R. (2014). Impact of period and timescale of FDDA analysis nudging on the numerical simulation of tropical cyclones in the Bay of Bengal. *Natural Hazards*, 74(3), 2109–2128. <https://doi.org/10.1007/s11069-014-1293-2>
- Zhao, P., Xu, X., Chen, F., Guo, X., Zheng, X., Liu, L., et al. (2018). The Third Atmospheric Scientific Experiment for Understanding the Earth–Atmosphere Coupled System over the

- 904 Tibetan Plateau and Its Effects. *Bulletin of the American Meteorological Society*, 99(4),
905 757–776. <https://doi.org/10.1175/BAMS-D-16-0050.1>
- 906 Zhao, P., Li, Y., Guo, X., Xu, X., Liu, Y., Tang, S., et al. (2019). The Tibetan Plateau Surface-
907 Atmosphere Coupling System and Its Weather and Climate Effects: The Third Tibetan
908 Plateau Atmospheric Science Experiment. *Journal of Meteorological Research*, 33(3),
909 375–399. <https://doi.org/10.1007/s13351-019-8602-3>
- 910 Zheng, D., Velde, R. V. der, Su, Z., Wen, J., Booij, M. J., Hoekstra, A. Y., & Wang, X. (2015).
911 Under-canopy turbulence and root water uptake of a Tibetan meadow ecosystem modeled
912 by Noah-MP. *Water Resources Research*, 51(7), 5735–5755.
913 <https://doi.org/10.1002/2015WR017115>
- 914 Zheng, D., Velde, R. V. der, Su, Z., Wen, J., Wang, X., Booij, M. J., et al. (2016). Impacts of
915 Noah model physics on catchment-scale runoff simulations. *Journal of Geophysical*
916 *Research: Atmospheres*, 121(2), 807–832. <https://doi.org/10.1002/2015JD023695>
- 917 Zhu, P., Albrecht, B. A., Ghate, V. P., & Zhu, Z. (2010). Multiple-scale simulations of
918 stratocumulus clouds. *Journal of Geophysical Research*, 115(D23), D23201.
919 <https://doi.org/10.1029/2010JD014400>